

## Microstructure and mechanism of in-situ $\text{Al}_2\text{O}_3(\text{p})/\text{Al}$ nano-composites synthesized by sonochemistry melt reaction

CHEN Deng-bin<sup>1</sup>, ZHAO Yu-tao<sup>1</sup>, ZHU Hai-yan<sup>2</sup>, ZHENG Meng<sup>1</sup>, CHEN Gang<sup>1</sup>

1. School of Materials Science and Engineering, Jiangsu University, Zhenjiang 212013, China;

2. Silicon Lake College, Kunshan 215332, China

Received 25 February 2011; accepted 23 June 2011

**Abstract:** The  $\text{Al}_2\text{O}_3(\text{p})/\text{Al}$  nano-composites were fabricated from  $\text{Al}-\text{K}_2\text{ZrF}_6-\text{Na}_2\text{B}_4\text{O}_7$  system by sonochemistry in situ reaction. The fabrication mechanisms, including high intensity ultrasonic influence on microstructures and reinforcement particles-aluminum matrix interface, were investigated by X-ray diffraction (XRD), scanning electron microscopy (SEM) and transmission electron microscopy (TEM). The XRD results show that the component of the as-prepared composites is  $\text{Al}_2\text{O}_3$  reinforcement. The SEM analysis results indicate that  $\text{Al}_2\text{O}_3$  particles are uniformly distributed in the aluminum matrix. The TEM results show that the morphologies of  $\text{Al}_2\text{O}_3$  particles present in nearly sphere-shape, the sizes are in the range of 20–100 nm, and the interfaces are net and no interfacial outgrowth is observed. Analysis with secondary development Image-J software shows that  $\text{Al}_2\text{O}_3$  recoveries are firstly improved and then decreased with increasing ultrasonic power. When the power is 0.4 kW, the distribution is the best, and a maximum number of particles are obtained. The reaction mechanisms were investigated.

**Key words:** sonochemistry; nano-composites; in situ reaction; reaction mechanism

### 1 Introduction

Due to light density, high specific strength and stiffness, high wear resistance and favorable dimensional stability, particulate reinforced aluminum matrix composites (PRAMCs) exhibit excellent comprehensive properties, and are widely used in aerospace, automotive manufactory and other fields [1–3]. Properties of this kind of composites rely largely on the distribution, morphology and size of reinforcement particles within aluminum matrix [4]. However, the size of the most popular and widely used reinforced particles at present is in a range of 3–30  $\mu\text{m}$  [5]. The results [6] show that the smaller size of reinforcement enhanced better. But the small particles not only have very few structural defects, but also have higher thermal mismatch dislocation density. Nano-particles have size effect, local field effect, quantum effect and surface effect, showing large difference with macro-composite material in the mechanical, thermal, electromagnetic and optical

properties. So, they are an ideal reinforcement [7]. But small particles easily join to form a so-called “nano-reinforced phase segregation zone”, then lead to the strengthening effect greatly reduced. While numerous methods (such as SHS, XD) [8, 9] have been offered for the fabrication of nano-composites, which involves adding reactants into molten aluminum, i.e., direct melt reaction (DMR) process, which is rarely reported.

In the present work, the  $\text{Al}_2\text{O}_3(\text{p})/\text{Al}$  nano-composites are fabricated from  $\text{Al}-\text{K}_2\text{ZrF}_6-\text{Na}_2\text{B}_4\text{O}_7$  system by in situ reaction. The microstructure, and the interface behaviors between the reinforcement particles and aluminum matrix are investigated by SEM and TEM. The reaction mechanisms are discussed.

### 2 Experimental

The raw materials were commercial aluminum ingots (purity  $\geq 99.8\%$ ), inorganic salt  $\text{K}_2\text{ZrF}_6$  and  $\text{Na}_2\text{B}_4\text{O}_7 \cdot 10\text{H}_2\text{O}$  powder (average size 20  $\mu\text{m}$ ). Table 1 shows the normal composition of the experimental

**Foundation item:** Project (50971066) supported by the National Natural Science Foundation of China; Project (20070299004) supported by the Research Fund for the Doctoral Program of Higher Education of China; Project (2008-46) supported by the Jiangsu Provincial ‘333’ Project of training the High-level Talents Foundation, China; Project (BE2009127) supported by the Jiangsu Provincial Science Supporting Item, China

**Corresponding author:** CHEN Deng-bin; Tel: +86-15952813450; E-mail: [cdb521\\_1984@163.com](mailto:cdb521_1984@163.com); ZHAO Yu-tao; E-mail: [zhaoyt@ujs.edu.cn](mailto:zhaoyt@ujs.edu.cn)  
DOI: 10.1016/S1003-6326(11)61136-9

**Table 1** Normal composition of experimental  $K_2ZrF_6$  and  $Na_2B_4O_7 \cdot 10H_2O$  powder

Raw material	Composition
$Na_2B_4O_7 \cdot 10H_2O$ powder	$w(Ca) \leq 0.005\%$
	$w(Cu) \leq 0.001\%$
	$w(Chloride) \leq 0.002\%$
	$w(Sulfate) \leq 0.01\%$
	$w(Phosphate) \leq 0.002\%$
	$Na_2B_4O_7 \cdot 10H_2O$ balance
$K_2ZrF_6$ powder	$w(H_2O) \leq 0.1\%$
	$w(Fe_2O_3) \leq 0.05\%$
	$K_2ZrF_6$ balance

inorganic salt  $K_2ZrF_6$  and  $Na_2B_4O_7 \cdot 10H_2O$ .

Firstly, the experimental inorganic salt  $K_2ZrF_6$  and  $Na_2B_4O_7 \cdot 10H_2O$  powder were dehydrated at 423 K for 3 h in an electric furnace. Secondly, the aluminum ingots were heated at 6 °C/min in a graphite crucible (with the inner diameter of 70 mm, the height of 160 mm and the single wall of 7.5 mm) which was set in a resistance furnace. The dried  $K_2ZrF_6$  and  $Na_2B_4O_7$  powders (mole ratio 3:1) with the mass fraction of 12% to the total melt were added when the melt was over-heated up to 1123 K. To avoid salt floatation, a campanulate graphite plunge was used to induce the salt mixture into the aluminum melt. Then, the cylindrical amplitude lever, which was made of titanium, was immersed into the aluminum melt to about 5 mm in depth. The ultrasonic generation system was turned on. For each experiment, the ultrasonic power was 0.2 kW, 0.4 kW, 0.6 kW. After 2 min of ultrasonic treatment, the melt was degassed by hexachloroethane degasifying agent, deslagged, and then was poured into a copper module when the melt was cooled to 993–1003 K.

Differential scanning calorimetry (DSC, STA449C) was used to estimate the reaction initiation temperature. X-ray diffraction (Dmax2500PC) using  $Cu K_\alpha$  radiation was used to determine phase component of the specimens. Scanning electron microscopy (SEM, JSM-7001F) was used to analyze the microstructure of the as-prepared specimens and TEM (JSM 2010) for morphologies and the interfaces. The particle and the particle volume fraction ( $\varphi$ ) were measured by Image-J software which was further developed by research group based on the combination of image analysis method and enrichment method with a large amount of experimental data.

### 3 Results and discussion

#### 3.1 Microstructures

Figure 1 shows the distributions and morphologies of dispersion phase. As shown in Fig. 1, the in situ

particles are distributed uniformly in the matrix; the morphology is nearly sphere-shape and the sizes are in the range of 20–100 nm. The enrichment method, which dissolves the as-prepared composite in 3%–5% hydrochloric acid solution to extract and XRD analysis, was utilized to confirm the composition of nano size dispersion phase. As shown in Fig. 2,  $Al_2O_3$  reinforcement phase is obtained in the present work.

Figure 3 shows TEM morphology of the in situ particles in the aluminum matrix. As shown in Fig. 3(a),

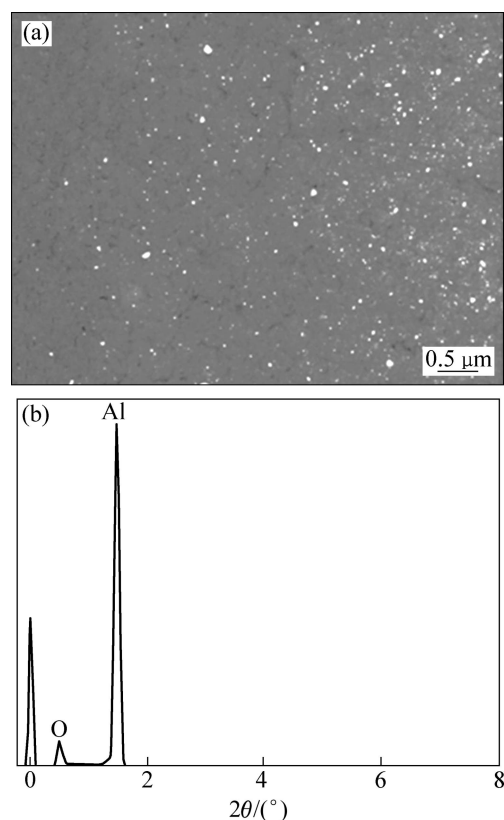


**Fig. 1** SEM image of as-prepared composite (a) and EDS analysis for white colored particles from Al- $K_2ZrF_6$ - $Na_2B_4O_7$  system (b)

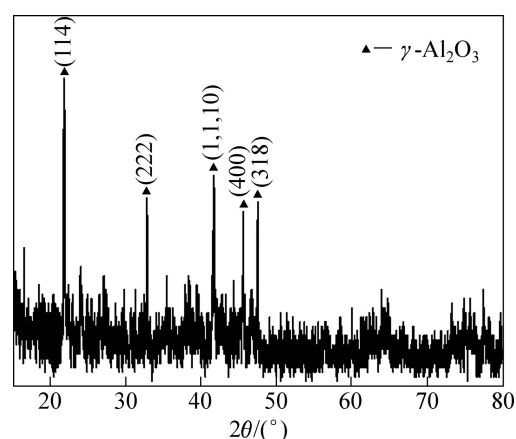


**Fig. 2** XRD pattern of extracted powder from Al- $K_2ZrF_6$ - $Na_2B_4O_7$  system

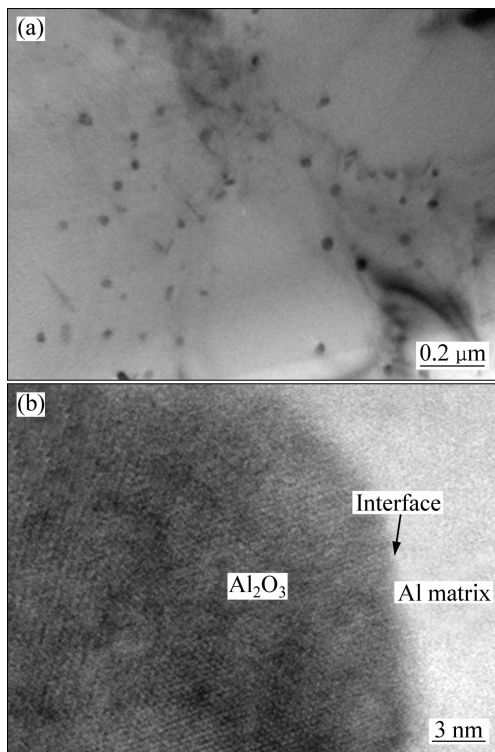


**Fig. 3** TEM image showing crystal morphology (a) and HRTEM image at interface of  $(\text{Al}_2\text{O}_3)_p/\text{Al}$  composite (b) from  $\text{Al-K}_2\text{ZrF}_6\text{-Na}_2\text{B}_4\text{O}_7$  system

the morphology of in situ particle is nearly ball-shape and the sizes are in the range of 20–100 nm. Figure 3(b) shows HRTEM image at the interface between in situ particle and Al matrix. The bright area could be identified as Al matrix, and the darker area is  $\text{Al}_2\text{O}_3$  via the digital micrograph software analysis. Furthermore, the interface between Al matrix and in situ particle is net and there is no resultant production observed.

### 3.2 Effect of $\text{K}_2\text{ZrF}_6$ addition

#### 3.2.1 Effect of $\text{K}_2\text{ZrF}_6$ addition on initial reaction temperature

Figure 4 shows the typical DSC plots for the stoichiometric powder mixture of  $\text{K}_2\text{ZrF}_6$ ,  $\text{Na}_2\text{B}_4\text{O}_7$  and Al heated at  $10^\circ\text{C}/\text{min}$ . As shown in Fig. 4, the thermograms show an endothermic peak corresponding to melting of aluminum nearby  $663.8^\circ\text{C}$ . Subsequently, a sharp exothermic peaks appear at  $1016.6^\circ\text{C}$ ,  $833.3^\circ\text{C}$ , respectively, which indicates the heat evolution due to the chemical reaction. From the DSC plot, the initiation temperature is found to be  $943.3^\circ\text{C}$  without  $\text{K}_2\text{ZrF}_6$  addition, largely higher than that with  $\text{K}_2\text{ZrF}_6$  addition. It reveals that the addition of  $\text{K}_2\text{ZrF}_6$ , to a great extent affects the reaction thermodynamics, which allows obtaining  $\text{Al}_2\text{O}_3$  particle at lower temperature comparing with reaction initiation temperature of  $943.3^\circ\text{C}$ .

#### 3.2.2 Effect of $\text{K}_2\text{ZrF}_6$ addition on reaction process

Figure 5 shows XRD patterns of the dross skimmed

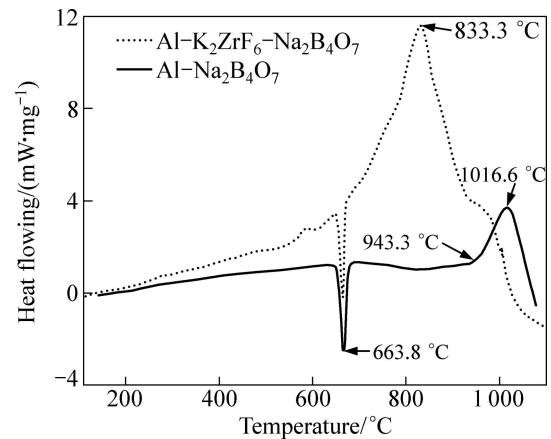
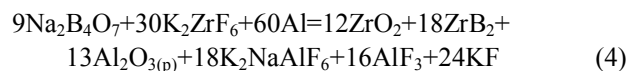


**Fig. 4** DSC analysis for addition of different reactants

from the melt. It reveals that the components of the dross predominantly consist of  $\text{ZrB}_2$ ,  $\text{AlF}_3$ ,  $\text{K}_2\text{NaAlF}_6$ , and  $\alpha(\text{Al})$  phases besides  $\text{Al}_2\text{O}_3$  and  $\text{ZrO}_2$ .  $\text{Al}_2\text{O}_3$  and  $\text{ZrO}_2$  reflections are very weak and the  $\text{K}_3\text{AlF}_6$  of the spent salt is completely replaced by  $\text{K}_2\text{NaAlF}_6$ . Thus, possible reaction can be inferred according to reaction products, which are described as follows [10]:



Due to no evidence for  $\text{Na}_2\text{O}$ , the overall reaction, leading to the formation of  $\text{ZrB}_2$  and  $\text{Al}_2\text{O}_3$  particles, upon the addition into molten aluminum, of  $\text{K}_2\text{ZrF}_6$  and  $\text{Na}_2\text{B}_4\text{O}_7$  mixture could be rewritten as:



It is suggested [11] that KF could react with Al as described by



The XRD analysis convincingly shows that a fraction of  $\text{Al}_2\text{O}_3$  particles are entrapped inside the spent salt, leading to lower  $\text{Al}_2\text{O}_3$  particle recoveries in aluminum matrix in some degree. As shown in Fig. 5, dross skimmed from the melt contains large amounts of  $\text{ZrB}_2$  particle, which well explains no  $\text{ZrB}_2$  particle in aluminum matrix. It is further confirmed that the reinforcement of as-prepared composite contains only  $\text{Al}_2\text{O}_3$  particle, and there is no evidence for the presence of other phases.

On the other hand, according to reactions (1)–(3),  $\text{K}_2\text{ZrF}_6$  reacts with Al to yield K–Al fluorides, which can be seen as KF– $\text{AlF}_3$  molten salt system, and greatly affect the reaction process. As a low temperature electrolysis, KF– $\text{AlF}_3$  molten salt system is widely used in electrolytic aluminum industry, to partly replace

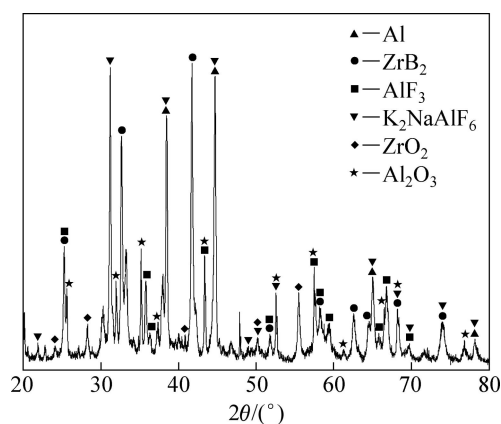


Fig. 5 XRD pattern for cross skimmed from melt

traditional NaF–AlF<sub>3</sub> molten salt system, because of its higher alumina solubility [12]. Reference [13] indicated that alumina solubility in KF–AlF<sub>3</sub> molten salt system could be high up to nearly 9% (mass fraction) and decrease with reduction of KF content. Thus, in our experimental condition, alumina dissolved in KF–AlF<sub>3</sub> molten salt system in early stage, and in subsequent, precipitated due to decrease of solubility caused by reduction of KF.

### 3.3 Influence of high intensity ultrasonic

#### 3.3.1 Influence of high intensity ultrasonic on microstructure

Figure 6 shows the influence of high intensity ultrasonic on the microstructures of the in situ Al<sub>2</sub>O<sub>3(p)</sub>/Al nano-composites by SEM. As shown in Fig. 6, the particle size is reduced and the number is increased with the assistance of the high intensity ultrasonic field. When the ultrasonic power is 0.4 kW, the Al<sub>2</sub>O<sub>3</sub> recovery reaches the maximum value of 90%, which is nearly 2.6 times relative to that without ultrasonic assistance. This is due to the cavitations effects and acoustic streaming effects from the high intensity ultrasonic field, which is beneficial to prevent from growth of particle and improve distribution. Furthermore, the acoustic streaming effects also give rise to considerable agitation of the melt which improves significantly the diffusion between reactants, leading to higher reaction efficiency.

#### 3.3.2 Influence of high intensity ultrasonic on Al<sub>2</sub>O<sub>3</sub> recovery

The Al<sub>2</sub>O<sub>3</sub> particle yields via reaction between K<sub>2</sub>ZrF<sub>6</sub>, Na<sub>2</sub>B<sub>4</sub>O<sub>7</sub> mixture powder and molten aluminum with varying levels of ultrasonic largely depending on the reaction efficiency of the mixture. Under the same experimental condition, Al<sub>2</sub>O<sub>3</sub> recovery ( $x$ ) can be defined by

$$x = \frac{\varphi_0}{\varphi_1} \quad (6)$$

where  $\varphi_0$  is the obtained particle volume fraction of Al<sub>2</sub>O<sub>3</sub>;  $\varphi_1$  is the intended particle volume fraction of Al<sub>2</sub>O<sub>3</sub>.

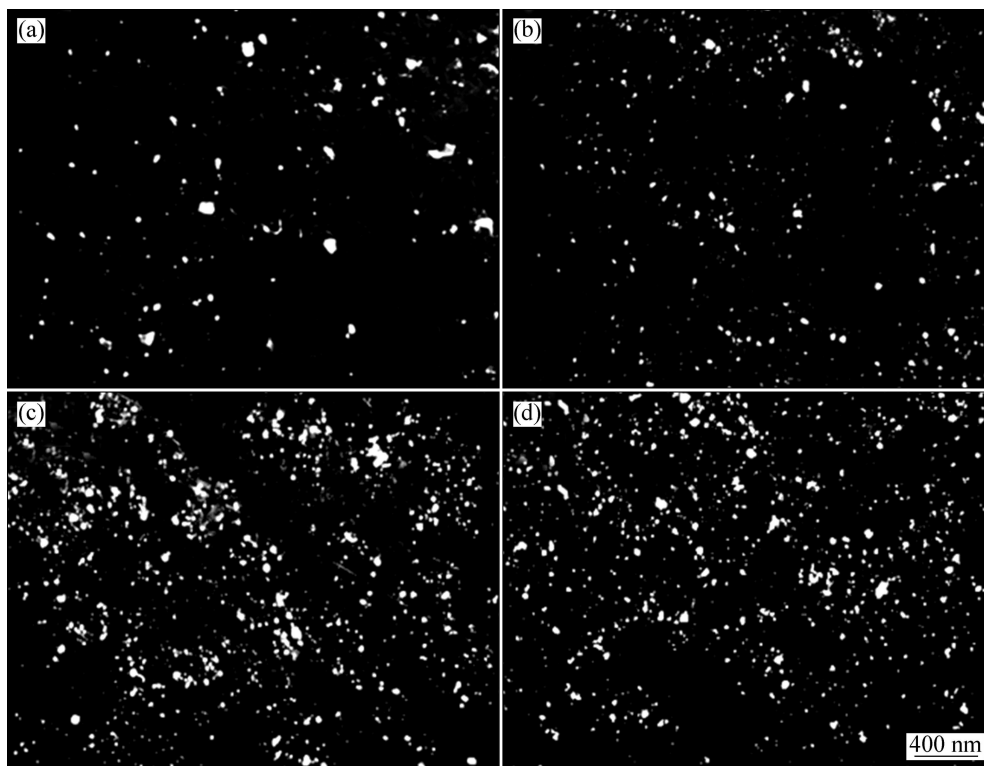


Fig. 6 Microstructures of Al<sub>2</sub>O<sub>3(p)</sub>/Al nano-composites treated by ultrasonic field with different powers: (a) 0 kW; (b) 0.2 kW; (c) 0.4 kW; (d) 0.6 kW

Figure 7 shows variation in  $\text{Al}_2\text{O}_3$  recovery as a function of ultrasonic power. It can be clearly seen that  $\text{Al}_2\text{O}_3$  recovery is improved with increasing ultrasonic power. Especially, when the ultrasonic power is 0.4 kW, the  $\text{Al}_2\text{O}_3$  recovery reaches the maximum value of 90%, which is nearly 2.6 times relative to that without ultrasonic treatment. But,  $\text{Al}_2\text{O}_3$  recovery decreases slightly with further increasing ultrasonic power when the ultrasonic power is more than 0.4 kW.

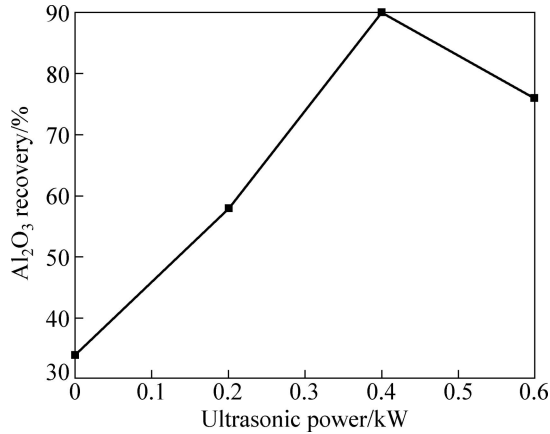


Fig. 7 Variation in  $\text{Al}_2\text{O}_3$  recovery as function of ultrasonic power

### 3.4 Mechanism of sonochemistry melt reaction

In the static melt, the spherical particle sedimentation caused by gravity can be expressed as:

$$u_t = \frac{d^2(\rho_s - \rho)g}{18\eta} \quad (7)$$

where  $u_t$  is the free settling velocity of particle;  $d$  and  $\rho_s$  are diameter and density for particle, respectively;  $\rho$  and  $\eta$  are the density and viscosity for composite melt, respectively.

Regardless of particle size, generally considering the role of particle volume fraction, the viscosity of static and low concentration suspension is described by Einstein polynomial [14]:

$$\frac{\eta}{\eta_0} = 1 + 2.5C + 10.5C^2 + 0.00273 \exp(16.6C) \quad (8)$$

where  $\eta$  is the viscosity of composite melt;  $\eta_0$  is the viscosity of matrix melt;  $C$  is the particle fraction.

In our experimental conditions,  $\eta_0 = 3.6 \times 10^{-4}$  Pa·s,  $C = 0.03$ . The viscosity of composite melt is thus calculated as  $\eta = 3.9 \times 10^{-4}$  Pa·s. Using Eq. (8), the free settling velocity of particle is calculated as  $u_t = 3.28 \times 10^{-7}$  m/s. Thus, particle sedimentation caused by gravity could be neglected.

Therefore, according to Ref. [15], the minimum sound energy density ( $E_{\min}$ ) required for particles moved

to acoustic pressure node or antinode could be expressed as:

$$E_{\min} = \frac{|\rho_p - \rho_l|g}{6\pi G} \lambda \quad (9)$$

And approximate solution of the time for particles reaching equilibrium state can be expressed as:

$$t = \frac{3\mu_1 c_1^2}{(2\pi/d_p)^2 EG} \ln \left| \frac{\tan kx_0}{\tan kx_f} \right| \quad (10)$$

where  $\rho_p$  and  $\rho_l$  are densities of particle and melt, respectively;  $G$  is acoustic contrast factor;  $\lambda$  is the sound wavelength;  $c_1$  is the speed of sound in melt;  $d_p$  is the diameter of particle;  $x_0$  is the distance from particle to acoustic pressure node for initial state;  $x_f$  is the distance from particle to acoustic pressure node for equilibrium state.

Equation (10) shows that the time required for particle to reach equilibrium state is inversely proportional to sound energy density, while sound energy density increases with ultrasonic power increasing. Thus,  $t$  is inversely proportional to ultrasonic power. In other words, the greater the ultrasonic power, the shorter the time required for particle to reach equilibrium state. Therefore, with the same treatment time in our experiment, particle reached equilibrium state more easily at higher ultrasonic power, and more likely to be removed as impurity, resulting in the  $\text{Al}_2\text{O}_3$  recovery decrease.

## 4 Conclusions

1) The  $\text{Al}_2\text{O}_3(\text{p})/\text{Al}$  nano-composites were successfully fabricated from  $\text{Al-K}_2\text{ZrF}_6\text{-Na}_2\text{B}_4\text{O}_7$  system by in situ reaction.

2) The reinforced phase in the as-prepared composites is  $\text{Al}_2\text{O}_3$  and there is hardly any evidence for  $\text{ZrB}_2$ . The morphologies of  $\text{Al}_2\text{O}_3$  particles present in nearly sphere-shape and the sizes are in the range of 20–100 nm. The interface between the reinforcement particles and aluminum matrix is net and no interfacial outgrowth is observed.

3) Addition of  $\text{K}_2\text{ZrF}_6$ , to a great extent, affects the reaction thermodynamics, and allows obtaining  $\text{Al}_2\text{O}_3$  particle at lower temperature comparing with that without  $\text{K}_2\text{ZrF}_6$  addition.

4) The  $\text{Al}_2\text{O}_3$  recovery reaches the maximum value of 90%, which is nearly 2.6 times relative to that without ultrasonic treatment when the ultrasonic power is 0.4 kW.

5) The formation mechanism of nano-size  $\text{Al}_2\text{O}_3$  particle is reaction-solution-precipitation.

## References

- [1] FAN Tong-xiang, ZHANG Di, YANG Guang, TOSHIYA S, MASSAKI N. Fabrication of in situ  $\text{Al}_2\text{O}_3/\text{Al}$  composite via remelting [J]. *Journal of Materials Processing Technology*, 2003, 142: 556–561.
- [2] KUMAR S, CHAKRABORTY M, SARMA V S, MURTY B S. Tensile and wear behaviour of in situ Al–7Si/TiB<sub>2</sub> particulate composites [J]. *Wear*, 2008, 265: 134–142.
- [3] ZAWRAH M F, ALY M H. In situ formation of  $\text{Al}_2\text{O}_3$ –SiC–mullite from Al-matrix composites [J]. *Ceramics International*, 2006, 32(1): 21–28.
- [4] WANG Hai-long, ZHANG Rui, HU Xing, WANG Chang-an, HUANG Yong. Characterization of a powder metallurgy SiC/Cu–Al composite [J]. *Journal of Materials Processing Technology*, 2008, 197: 43–48.
- [5] TANI T. Processing, microstructure and properties of in-situ reinforced SiC matrix composites [J]. *Composites: Part A*, 1999, 30: 419–423.
- [6] VARMA V K, KAMAT S V, MAHAJAN Y R, KUTUMBARAO V V. Effect of reinforcement size on low strain yielding behavior in Al–Cu–Mg/SiC<sub>p</sub> composites [J]. *Materials Science and Engineering A*, 2001, 318: 57–64.
- [7] SHAFIEI-ZARGHANI A, KASHANI-BOZORG S F, ZAREI-HANZAKI A. Microstructures and mechanical properties of Al/ $\text{Al}_2\text{O}_3$  surface nano-composite layer produced by friction stir processing [J]. *Materials Science and Engineering A*, 2008, 500: 84–91.
- [8] CAMURLU E H, MAGLIA F. Preparation of nano-size ZrB<sub>2</sub> powder by self-propagating high-temperature synthesis [J]. *Journal of the European Ceramic Society*, 2009, 29: 1501–1506.
- [9] ZHU He-guo, WANG Heng-zhi, GE Liang-qi. Wear properties of the composites fabricated by exothermic dispersion reaction synthesis in an Al–TiO<sub>2</sub>–B<sub>2</sub>O<sub>3</sub> system [J]. *Wear*, 2008, 264: 967–972.
- [10] YUCEL B. Production of Al–Ti–B grain refining master alloys from Na<sub>2</sub>B<sub>4</sub>O<sub>7</sub> and K<sub>2</sub>TiF<sub>6</sub> [J]. *Journal of Alloys and Compounds*, 2008, 458: 271–276.
- [11] JONAS F, ANDERS EW. On the precipitation of TiB<sub>2</sub> in aluminum melts from the reaction with KBF<sub>4</sub> and K<sub>2</sub>TiF<sub>6</sub> [J]. *Materials Science and Engineering A*, 2005, 413–414: 527–532.
- [12] XU Qian, MA Yi-ming, QIU Zhu-xian. Calculation of thermodynamic properties of LiF–AlF<sub>3</sub>, NaF–AlF<sub>3</sub> and KF–AlF<sub>3</sub> [J]. *Calphad*, 2001, 25: 31–42.
- [13] ZHANG Yun-hui, YIN Shu-mei, XIAO Li, LI Ning, ZHANG Ze-shen. Study on potassium fluoaluminate eutectic flux [J]. *Transactions of Tianjin University*, 2004, 10(3): 184–186.
- [14] LBYD D J. Solidification microstructure of particulate reinforced aluminum/SiC composites [J]. *Composites Science and Technology*, 1989, 35: 159–179.
- [15] CHEN Deng-bin, ZHAO Yu-tao, LI Gui-rong. Effects of high intensity ultrasonic on microstructure and mechanism of in-situ Al<sub>3</sub>Ti/6070 composites [J]. *The Chinese Journal of Nonferrous Metals*, 2009, 19(11): 1956–1961. (in Chinese)

## 超声化学原位合成 $\text{Al}_2\text{O}_3(\text{p})/\text{Al}$ 纳米复合材料的组织及其机理

陈登斌<sup>1</sup>, 赵玉涛<sup>1</sup>, 祝海燕<sup>2</sup>, 郑梦<sup>1</sup>, 陈刚<sup>1</sup>

1. 江苏大学 材料科学与工程学院, 镇江 212013;

2. 硅湖职业技术学院, 昆山 215332

**摘要:** 采用超声化学原位反应, 以 Al–K<sub>2</sub>ZrF<sub>6</sub>–Na<sub>2</sub>B<sub>4</sub>O<sub>7</sub> 为反应体系, 制备  $\text{Al}_2\text{O}_3(\text{p})/\text{Al}$  纳米复合材料。利用扫描电镜和透射电镜, 研究高能超声对复合材料组织和颗粒收得率的影响及加入 K<sub>2</sub>ZrF<sub>6</sub> 对反应过程以及增强颗粒与铝基体的界面的影响。X 射线衍射(XRD)、扫描电镜(SEM)与透射电镜(TEM)结果表明: 所制备的复合材料增强颗粒为  $\text{Al}_2\text{O}_3$ ,  $\text{Al}_2\text{O}_3$  颗粒在基体中分布均匀, 其形貌为近球形, 尺寸 20~100 nm, 界面干净且无界面产物。利用经过二次开发的 Image-J 软件对  $\text{Al}_2\text{O}_3$  颗粒收得率进行分析, 结果表明,  $\text{Al}_2\text{O}_3$  颗粒收得率随着超声功率的增大呈现出先增大后减小的变化规律。当超声功率达到 0.4 kW 时, 颗粒分布最好且数量最多。并对其反应机理也进行了探讨。

**关键词:** 超声化学; 纳米复合材料; 原位反应; 反应机理

(Edited by YANG Hua)